

Modeling and Simulation of the Cholesteric Landau–de Gennes Model

Andrew L. Hicks¹

*Department of Mathematics
Louisiana State University,
Baton Rouge, LA 70803*

Shawn W. Walker*

*Department of Mathematics
Center for Computation and Technology (CCT)
Louisiana State University,
Baton Rouge, LA 70803 Tel.: +1-225-578-1603
Fax: +1-225-578-4276*

Abstract

This paper presents an analysis of modeling and numerical issues in the Landau–de Gennes (LdG) model of nematic liquid crystals (LCs) with cholesteric effects. We derive various time-step restrictions for a (weighted) L^2 gradient flow scheme to be energy decreasing. Furthermore, we prove a mesh size restriction, for finite element discretizations, that is critical to avoid spurious numerical artifacts in discrete minimizers that is not well-known in the LC literature, particularly when simulating cholesteric LCs that exhibit “twist.”

Furthermore, we perform a computational exploration of the model and present several numerical simulations in 3-D, on both slab geometries and spherical shells, using a fully-implicit gradient flow scheme applied to a finite element discretization of the model. The simulations are consistent with experiments, illustrate the richness of the cholesteric model, and demonstrate the importance of the mesh size restriction.

Keywords: liquid crystals, Landau–de Gennes, finite element method, cholesteric, gradient flow

2010 MSC: 65M60, 65N30, 65N15, 49M20, 35J61, 35K58

*Corresponding author; S. W. Walker acknowledges financial support by the NSF DMS-1555222 (CAREER).

Email addresses: ahick17@lsu.edu (Andrew L. Hicks), walker@math.lsu.edu (Shawn W. Walker)

1. Introduction

New types of materials are a necessary component in many new technologies [1, 2]. Liquid crystals (LCs), in particular, are finding innovative uses in many material design problems. Originally, nematic LCs were developed and commercialized for their optical properties [3, 4, 5, 6, 7, 8], which is what enables LC displays.

Many nematic LCs are characterized by several material constants [9, 10], which provide useful tuning parameters that can be tailored to specific applications. This paper is concerned with the modeling and numerical simulation of a particular sub-type of LC which are known as cholesteric nematic LCs, where the molecules have a chiral structure that affects their actuation and equilibrium behavior [3, 11, 12]. Cholesteric LCs are present in many biological systems, such as viruses [13], chitin [14], and the structured coloring of the scarab beetle [15]. These materials often exhibit stripe patterns in their optical response, which can be exploited for engineering materials for the built environment [16, 17]. This paper presents a numerical method and analysis for simulating cholesteric LCs in order to predict their structural features. Numerical modeling can yield greater insight into the functional effects of cholesteric LCs in biological systems and enable the design of programmable materials [18, 19, 20].

Many numerical methods and implementations exist for the standard LdG model, e.g. [21, 22, 23, 24, 25, 26, 27, 28]. These methods have also been extended to tackle cholesteric LCs [29, 30, 11, 12]. However, to the best of our knowledge, a proper numerical analysis of the general LdG model that includes the cholesteric term appears to be lacking.

This paper gives an overview of numerical analysis issues that can arise in the general Landau-de Gennes model with cholesteric effects. We address both computing L^2 gradient flow dynamics, as well as solving the equilibrium equations that characterize a local minimizer. In particular, time-step restrictions are needed to guarantee energy decrease of the gradient flow (e.g., even for the well-known convex-splitting scheme for handling the bulk potential). In addition, a mesh-size restriction appears that is not immediately obvious, i.e. if the computational mesh size is not small enough, unphysical solutions may occur (i.e. the computed local minimizer may exhibit numerical artifacts). Furthermore, we investigate two slightly different cholesteric models which can potentially produce very different results. We also demonstrate that the choice of initial condition can significantly affect which local minimizer is found, as well as the speed of convergence to a solution.

Part of the contribution of this paper is to present these issues, and how to handle them, to a diverse audience of computational scientists. Another contribution is to explore the cholesteric LdG model and illustrate the rich phenomena that result from it; see [17, 12, 11] for related work. Our presentation here should enable more robust computations for exploring the LC physics and device design of systems that are governed by the cholesteric Landau-de Gennes model.

We summarize some notational conventions we use in this paper. We focus

on three dimensional liquid crystal models; thus 2-tensors are elements of $\mathbb{R}^{3 \times 3}$ denoted by standard capital letters, e.g. the 3×3 identity tensor is written as I . Constants and scalar-valued functions will be denoted by lowercase letters. Moreover, Greek letters will typically denote certain important functions and constants. Vectors will be denoted by boldface lowercase letters.

Let the D operator denote differentiation of a scalar-valued function with respect to each argument of a tensor; that is, for any function ϕ mapping to \mathbb{R} , define

$$D\phi(P) := \left[\frac{\partial \phi}{\partial P_{ij}} \right]_{i,j=1}^3, \quad D^2\phi(P) := \left[\frac{\partial^2 \phi}{\partial P_{ij} \partial P_{kl}} \right]_{i,j,k,l=1}^3, \quad \forall P \in \mathbb{R}^{3 \times 3},$$

i.e. the gradient and Hessian operators. For derivatives with respect to spatial coordinates, we use $\partial_i \phi := \partial_{x_i} \phi$, where $\mathbf{x} = (x_1, x_2, x_3)^\dagger$ is the spatial coordinate, or we use the comma-subscript notation, e.g. $\phi_{,i} := \partial_i \phi$ and $P_{ij,k} := \partial_k P_{ij}$.

Next, we define the $L^2(\Omega)$, $L^2(\Gamma)$ inner products and associated norms:

$$(A, B)_\Omega := \int_\Omega (A, B) d\mathbf{x}, \quad \|A\|_{0,\Omega}^2 := (A, A)_\Omega,$$

$$(A, B)_\Gamma := \int_\Gamma (A, B) dS(\mathbf{x}), \quad \|A\|_{0,\Gamma}^2 := (A, A)_\Gamma,$$

where A, B could be scalars, vectors, or tensors, and (\cdot, \cdot) the inner product between them is the dot product of scalars, vectors, or tensors, respectively. We also have the $H^1(\Omega)$ norm: $\|P\|_{1,\Omega}^2 := \|P\|_{0,\Omega}^2 + \|\nabla P\|_{0,\Omega}^2$.

2. Liquid Crystal Theory

We briefly review the Landau-de Gennes theory for a nematic LC phase.

2.1. Coarse-grained Molecular Theory

LCs are a *meso-phase* of matter where the ordered macroscopic state is between a spatially disordered liquid and a fully crystalline solid [31]. Nematic LC molecules are rod-like and are free to slide about, meaning no positional order is maintained. The (partial) spatial order that is maintained is *orientational*, i.e. the rod-like molecules prefer to be aligned with their neighbors due to molecular forces.

The Q -tensor order parameter, which represents the orientational order, can be derived via first principles (see [31]). Given a domain Ω containing liquid crystals, Q is a tensor-valued function over Ω where $Q(\mathbf{x})$ represents the (statistical) state of the liquid crystal (at \mathbf{x}) and belongs to

$$\mathbf{S}_0 := \{Q \in \mathbb{R}^{3 \times 3} \mid Q^\dagger = Q, \text{tr}(Q) = 0\}. \quad (1)$$

Next, writing Q in its eigenframe, we have $Q = \sum_{i=1}^3 \lambda_i \mathbf{e}_i \otimes \mathbf{e}_i$, where $\lambda_i \equiv \lambda_i(Q)$ are the eigenvalues of Q , and \mathbf{e}_i are the normalized eigenvectors. From the

properties of Q , one can show that each λ_i satisfies $-(1/3) \leq \lambda_i(Q) \leq (2/3)$ (for $i = 1, 2, 3$). Also, since Q is traceless, $\lambda_3 = -(\lambda_1 + \lambda_2)$. If all eigenvalues are equal, they are 0 and we simply have $Q = 0$, which represents the isotropic state (no nematic order). Likewise, when all eigenvalues are different from one another, we have what is called the biaxial state. Most commonly, when only two of the eigenvalues are equal, we have the so-called *uniaxial* state, where Q may be expressed as

$$Q = s \left(\mathbf{n} \otimes \mathbf{n} - \frac{1}{3} I \right), \quad (2)$$

where s is called the *degree-of-orientation*, and is a measure of the orientational order of the LC molecules at each point, and \mathbf{n} is called the *director*, which has unit length, $|\mathbf{n}| = 1$, and represents the average direction in which the molecules are pointing. One can show that $-\frac{1}{2} \leq s \leq 1$. For many nematic LCs, the default state is usually uniaxial with a particular value of s that depends on the material. Typically, the optimal s is in the range $0.5 \leq s \leq 0.8$ [3].

2.2. Landau-de Gennes Theory

Next, we model the state of an LC system through a tensor-valued function $Q : \Omega \rightarrow \mathbf{S}_0$, where Ω is the physical domain of interest. We assume throughout that Ω has Lipschitz boundary Γ with outward pointing unit normal vector $\boldsymbol{\nu}$ (e.g. box-like domains and domains with smooth boundary are allowed). We assume that the equilibrium state of the LC is represented by a function Q that (locally) minimizes the LdG free energy [9, 10, 29]:

$$\begin{aligned} \mathcal{E}[Q] := & \int_{\Omega} f(Q, \nabla Q) d\mathbf{x} + \int_{\Omega} \psi(Q) d\mathbf{x} + \int_{\Gamma} g(Q) dS(\mathbf{x}) \\ & + \int_{\Gamma} \phi(Q) dS(\mathbf{x}) - \int_{\Omega} \chi(Q) d\mathbf{x}, \end{aligned} \quad (3)$$

with the elastic energy (with twist component as in [11, 29]) given by

$$f(Q, \nabla Q) := \frac{1}{2} \left(\ell_1 |\nabla Q|^2 + \ell_2 |\nabla \cdot Q|^2 + \ell_3 (\nabla Q)^{\dagger} : \nabla Q + 4\ell_1 \tau_0 \nabla Q : (\varepsilon \cdot Q) \right), \quad (4)$$

where $\{\ell_i\}_{i=1}^3$ (units of J/m) and τ_0 (units of m⁻¹) are material dependent elastic constants, and we have the (frame indifferent) invariants $|\nabla Q|^2 := Q_{ij,k} Q_{ij,k}$, $|\nabla \cdot Q|^2 := Q_{ij,j} Q_{ik,k}$, $(\nabla Q)^{\dagger} : \nabla Q := Q_{ij,k} Q_{ik,j}$, $\nabla Q : (\varepsilon \cdot Q) := \varepsilon_{jkl} Q_{ik,l} Q_{ij}$, where we use the convention of summation over repeated indices and ε_{jkl} is the Levi-Civita tensor. The transpose in the third term indicates to swap one of the Q indices with the derivative index. Note that taking $\ell_i = 0$, for $i = 2, 3$, and $\tau_0 = 0$ gives the often used one constant LdG model.

Next, the bulk potential ψ is a double-well type of function that is given by

$$\psi(Q) = a_0 - \frac{a_2}{2} \text{tr}(Q^2) - \frac{a_3}{3} \text{tr}(Q^3) + \frac{a_4}{4} (\text{tr}(Q^2))^2. \quad (5)$$

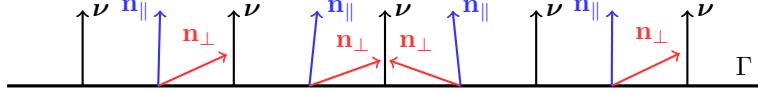


Figure 1: Homeotropic anchoring and planar degenerate anchoring are demonstrated in the above illustration. For homeotropic or normal anchoring, directors \mathbf{n}_{\parallel} are brought more in line with the outward normal directors $\boldsymbol{\nu}$. On the other hand, for planar degenerate anchoring, directors \mathbf{n}_{\perp} are aligned closer to being tangent to the surface. The closeness of alignment in either case is controlled by the constant w_0 or the constants w_1 and w_2 , respectively.

105 Above, a_2, a_3, a_4 are material parameters (units of J/m^3) such that a_2, a_3, a_4 are positive; a_0 is a convenient constant to ensure $\psi \geq 0$. Stationary points of ψ are either uniaxial or isotropic Q -tensors [32]. Combined with (2), the critical values of the scalar order parameter s for $\psi(Q(s))$, where $Q(s)$ is uniaxial, are $s = 0$ (local maximum), $s = (a_3 - \sqrt{a_3^2 + 24a_2a_4})/(4a_4)$ (local minimum) and
110 the global minimum [33]: $s_0 = (a_3 + \sqrt{a_3^2 + 24a_2a_4})/(4a_4)$, and is typically in the range $0.5 \leq s_0 \leq 0.8$ [3] for a_2 sufficiently large positive, which we shall always assume. Note that, for thermotropic LCs, a_2 is temperature dependent where a_2 can become a large negative parameter for high enough temperature [10, 31]. In this case, ψ becomes a convex function with a global minimum at
115 $Q = 0$ (the isotropic state). Though this potential is rather simplistic in that it does not guarantee that the eigenvalues of Q remain in the physical range (see earlier), it is effective in most modeling situations (c.f. [32]).

120 The surface energy, composed of the quadratic $g(Q)$ and higher-order $\phi(Q)$, accounts for *weak anchoring* of the LC (i.e. penalization of boundary conditions). For example, a Rapini-Papoulier type anchoring energy [34] can be considered:

$$g(Q) = \frac{w_0}{2}|Q - Q_{\Gamma}|^2 + \frac{w_1}{2}|\tilde{Q} - \tilde{Q}^{\perp}|^2, \quad \phi(Q) = \frac{w_2}{4}(|\tilde{Q}|^2 - s_0^2)^2, \quad (6)$$

125 where w_0, w_1 , and w_2 are positive constants (units of J/m^2), $Q_{\Gamma}(x) \in \mathbf{S}_0$ for all $x \in \Gamma$, and s_0 is the scalar order parameter of the uniaxial Q that minimizes the double well. We set $\tilde{Q} := Q + \frac{s_0}{3}I$, and define the standard projection onto the plane orthogonal to $\boldsymbol{\nu}$, that is, $Q^{\perp} := \Pi Q \Pi$ where $\Pi = I - \boldsymbol{\nu} \otimes \boldsymbol{\nu}$. We define Q_{Γ} to be uniaxial of the form $Q_{\Gamma} = s_0(\boldsymbol{\nu} \otimes \boldsymbol{\nu} - I/3)$. The w_0 term in (6) models homeotropic (normal) anchoring, while w_1 and w_2 model planar degenerate anchoring. See Figure 1 for an illustration.

130 The function $\chi(\cdot)$ accounts for interactions with external fields. For example, the energy density of a dielectric LC with fixed boundary potential is given by $-1/2 \mathbf{D} \cdot \mathbf{E}$ [35], where the electric displacement \mathbf{D} is related to the electric field \mathbf{E} by the linear constitutive law [36, 3, 37]: $\mathbf{D} = \boldsymbol{\varepsilon}\mathbf{E} = \bar{\varepsilon}\mathbf{E} + \varepsilon_a Q\mathbf{E}$, $\boldsymbol{\varepsilon}(Q) = \bar{\varepsilon}I + \varepsilon_a Q$, where $\boldsymbol{\varepsilon}$ is the LC material's dielectric tensor and $\bar{\varepsilon}, \varepsilon_a$ are constitutive dielectric permittivities. Thus, $-(1/2)\mathbf{D} \cdot \mathbf{E} = -(1/2)\bar{\varepsilon}|\mathbf{E}|^2 + \chi(Q)$, where
135 $\chi(Q) = -\frac{1}{2}\varepsilon_a \mathbf{E} \cdot Q\mathbf{E} \equiv -\frac{1}{2}\varepsilon_a \mathbf{E} \otimes \mathbf{E} : Q$, with units J/m^3 .

2.3. Non-dimensionalization

We start by noting that Q and s are already non-dimensional. Lengths and coordinates are non-dimensionalized by introducing a characteristic length ξ , e.g. $\hat{\mathbf{x}} = \mathbf{x}/\xi$, where $\hat{\mathbf{x}}$ is non-dimensional. Then, set ℓ_m to be the maximum or
¹⁴⁰ average of $\{|\ell_i|\}_{i=1}^3$ and simply divide (3) by $\ell_m \cdot \xi$ to obtain a dimensionless energy. This effectively rescales all spatial derivatives, integral measures, and the various constants in the problem. Other non-dimensionalizations are possible (c.f. [38, Sec. 2.]).

However, $\psi(Q)$ and $\phi(Q)$ are non-convex functions, which significantly affect
¹⁴⁵ the numerical analysis of the model. Thus, we describe their non-dimensionalization in more detail. Set $c_0 := \psi(0) - \psi(Q(s_0))$ and define the non-dimensional bulk potential by $\widehat{\psi}(Q) := \psi(Q)/c_0$; thus, $\widehat{\psi}(0) - \widehat{\psi}(Q(s_0)) = 1$. This immediately implies that $|D\widehat{\psi}(Q)| = O(1)$, as Q varies between the isotropic state and the global minimum of ψ . Then, upon introducing the non-dimensional parameter
¹⁵⁰ $\eta := \sqrt{\ell_m}/(c_0\xi^2)$, we have

$$\frac{1}{\ell_m \xi} \int_{\Omega} \psi(Q) d\mathbf{x} = \frac{1}{\eta^2} \int_{\widehat{\Omega}} \widehat{\psi}(Q) d\hat{\mathbf{x}}, \quad (7)$$

where $\widehat{\Omega}$ is the scaled domain. As for $\phi(Q)$, upon setting $\widehat{\phi}(Q) = (|\tilde{Q}|^2 - s_0^2)^2/4$ and $\omega := \ell_m/(w_2\xi)$, we have

$$\frac{1}{\ell_m \xi} \int_{\Gamma} \phi(Q) dS(\mathbf{x}) = \frac{1}{\omega} \int_{\widehat{\Gamma}} \widehat{\phi}(Q) d\hat{S}(\hat{\mathbf{x}}), \quad (8)$$

where $\widehat{\Gamma}$ is the scaled boundary. Then, the total non-dimensional energy is

$$\begin{aligned} \widehat{\mathcal{E}}[Q] &= \int_{\widehat{\Omega}} \widehat{f}(Q, \widehat{\nabla} Q) d\hat{\mathbf{x}} + \frac{1}{\eta^2} \int_{\widehat{\Omega}} \widehat{\psi}(Q) d\hat{\mathbf{x}} + \int_{\widehat{\Gamma}} \widehat{g}(Q) d\hat{S}(\hat{\mathbf{x}}) \\ &\quad + \frac{1}{\omega} \int_{\widehat{\Gamma}} \widehat{\phi}(Q) d\hat{S}(\hat{\mathbf{x}}) - \int_{\widehat{\Omega}} \widehat{\chi}(Q) d\hat{\mathbf{x}}. \end{aligned} \quad (9)$$

For simplicity, we drop the “hat” notation for the remainder of the paper.

¹⁵⁵ 2.4. The Cholesteric LdG Model

Cholesteric LCs are created by adding a chiral dopant (i.e. molecules with a chiral structure) to nematic LCs. This induces a helical superstructure on the nematic phase, which means the local behavior of the LC is nematic (i.e. line segments are aligned with their immediate neighbors) but the larger, super-molecular arrangement of the line segments follows a helical structure with a certain periodicity (or pitch), p . The physical manifestation of the cholesteric phase is that the helix modulates the optical properties in a periodic fashion.
¹⁶⁰

The cholesteric, LdG model in (3) can be obtained through a mapping procedure from the cholesteric, Oseen-Frank (director) LC model (see [9]). But we also consider a slightly different cholesteric model given in [11]. In the following sections, we relate this model (which we refer to as the cholesteric model) to the
¹⁶⁵

LdG model we have defined in Section 2.2. The elastic energy in [11] is, mainly, a rewriting of the terms in (4). However, there is an implicit interference of the elastic energy in [11] with the bulk potential that brings up a modeling issue we highlight in part 2.4.2 of this section.

2.4.1. Elastic energy

The cholesteric model in [11] gives the elastic energy as

$$f_{\text{grad}}(Q) = \left(\frac{\check{\ell}_1}{2}\right)|\nabla \times Q + 2\tau_0 Q|^2 + \left(\frac{\check{\ell}_2}{2}\right)|\nabla \cdot Q|^2 + \left(\frac{\check{\ell}_{24}}{2}\right)(Q_{ij,k}Q_{ik,j} - Q_{ij,j}Q_{ik,k}), \quad (10)$$

where $\check{\ell}_1$, $\check{\ell}_2$, $\check{\ell}_{24}$ are elastic constants, $\tau_0 = 2\pi/p$ with p being the pitch, and $\nabla \times Q = \varepsilon_{ikl}Q_{lj,k}\mathbf{e}^i \otimes \mathbf{e}^j$, where \mathbf{e}^i is the i th vector in the standard basis of \mathbb{R}^3 . This is referred to as the curl of Q and is consistent with the definition of curl for vectors, i.e. the columns of $\nabla \times Q$ are the curls of the corresponding columns of Q . The term $|\nabla \times Q + 2\tau_0 Q|^2$ is what frustrates the equilibrium state from having a constant director and models the chiral structure of the molecules. As we will see in the numerical results, choosing $\tau_0 > 0$ causes a “twisting” of the director throughout the LC domain.

It is a straightforward exercise in index notation to prove the identity $|\nabla \times Q|^2 = Q_{ij,k}Q_{ij,k} - Q_{ij,j}Q_{ik,j}$. Moreover, from the definition of $\nabla \times Q$, we have the identity $(\nabla \times Q) : Q = (\varepsilon_{ikl}Q_{lj,k}\mathbf{e}^i \otimes \mathbf{e}^j) : Q = \varepsilon_{ikl}Q_{lj,k}Q_{ij}$. With this, we can rewrite (10) in the form of (4) by first noting that

$$\begin{aligned} \left(\frac{\check{\ell}_1}{2}\right)|\nabla \times Q + 2\tau_0 Q|^2 &= \left(\frac{\check{\ell}_1}{2}\right)Q_{ij,k}Q_{ij,k} - \left(\frac{\check{\ell}_1}{2}\right)Q_{ij,k}Q_{ik,j} \\ &\quad + \left(\frac{4\check{\ell}_1}{2}\right)\tau_0\varepsilon_{ikl}Q_{lj,k}Q_{ij} + 2\check{\ell}_1\tau_0^2|Q|^2. \end{aligned}$$

From here, we note that $\text{tr}(Q^2) \equiv |Q|^2$, rearrange the terms and group them as:

$$\begin{aligned} f_{\text{grad}}(Q) &= \left(\frac{\check{\ell}_1}{2}\right)Q_{ij,k}Q_{ij,k} + \left(\frac{\check{\ell}_2 - \check{\ell}_{24}}{2}\right)Q_{ij,j}Q_{ik,k} \\ &\quad + \left(\frac{\check{\ell}_{24} - \check{\ell}_1}{2}\right)Q_{ij,k}Q_{ik,j} + \left(\frac{4\check{\ell}_1}{2}\right)\tau_0\varepsilon_{ikl}Q_{lj,k}Q_{ij} + 2\check{\ell}_1\tau_0^2\text{tr}(Q^2). \end{aligned} \quad (11)$$

We then use frame indifferent invariants to map these constants to the LdG elastic and twist energy densities as given in (4), i.e. $\ell_1 = \check{\ell}_1$, $\ell_2 = \check{\ell}_2 - \check{\ell}_{24}$, $\ell_3 = \check{\ell}_{24} - \check{\ell}_1$, where the twist constant τ_0 is the same in both models. Note that there is an extra term of $|Q|^2 \equiv \text{tr}(Q^2)$ in (11) that is *not* found in (4) but does appear in (5). We discuss the implications of this in the next subsection.

2.4.2. Alternative Cholesteric Model

In (4) and in [29], they consider the (cholesteric) elastic energy as not containing a $\text{tr}(Q^2)$ term like [11] does. Indeed, keeping this term can have a significant effect on the behavior of energy minimizers.

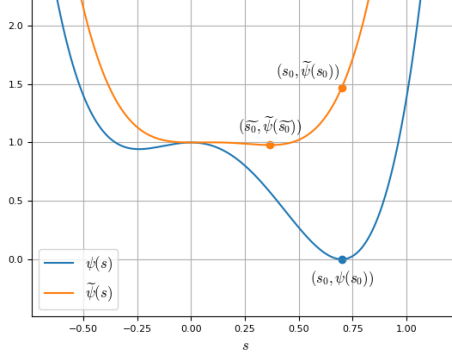


Figure 2: The two double wells from the two models. This compares the double well ψ in (5) to the effective double well $\tilde{\psi}$ in (12), which arises when the alternate cholesteric model is used. Notice that the global minima, s_0 for ψ and \tilde{s}_0 for $\tilde{\psi}$, of the two bulk potentials differ greatly.

195 For simplicity of exposition, we assume all energies have been non-dimensionalized, take $\ell_1 = 1$, $\tau_0 > 0$, and set the other elastic constants to zero. If we keep the $\text{tr}(Q^2)$ term in (11), it will combine with the a_2 coefficient in (5) to produce a new effective (non-dimensional) bulk potential in (9), namely

$$\tilde{\psi}(Q) = a_0 - \frac{a_2 - 4\ell_1\eta^2\tau_0^2}{2} \text{tr}(Q^2) - \frac{a_3}{3} \text{tr}(Q^3) + \frac{a_4}{4} (\text{tr}(Q^2))^2, \quad (12)$$

200 where $\tilde{a}_2 = a_2 - 4\eta^2\tau_0^2$ is the coefficient in front of $\text{tr}(Q^2)$. If $\tau_0 = 15$ and $a_2 = 1$, for instance, then choosing $\eta = 0.0408$ yields $\tilde{a}_2 \approx 0.5$, which is a significant change in the global minimum. One would have to choose $\eta = 0.01$ to have $\tilde{a}_2 > 0.9$. Moreover, if η is not small enough to compensate for τ_0 , then \tilde{a}_2 will be negative, which makes the $\text{tr}(Q^2)$ term positive. If \tilde{a}_2 is sufficiently large and negative, then $\tilde{\psi}(Q)$ will be a convex function, with a single minimum at $Q = 0$, implying that the isotropic phase is preferred. Figure 2 shows a comparison between the original double well and the modified one; clearly, the location of the global minima are different.

210 To the best of our knowledge, the material doping discussed at the beginning of Section 2.4, which is needed to create a cholesteric LC, should not change the nematic phase diagram, which is directly connected to the double well potential. Moreover, choosing η sufficiently small to reduce the interference with the bulk potential is computationally inconvenient because it makes the problem more stiff; smaller time-steps will be needed to ensure energy decrease in a gradient descent scheme. Therefore, we mainly adopt the approach in [29], which is justified in [9], and simply drop the $\text{tr}(Q^2)$ term in (11). But we do provide a comparison with the model in [11] in Section 5.6.

Remark 1. The surface anchoring energy proposed in [11] is the same as that given in (6) but with a trivial change in the constants.

3. Minimizing the Landau-de Gennes Energy

220 Existence of a minimizer of (9) can be established through the direct method of the calculus of variations; for instance, see [23]. Computing a minimizer can, in principle, be done by solving the Euler-Lagrange equations associated with (9) (i.e. the first order condition). However, these equations are non-linear and the energy is non-convex, so simply applying Newton's method will not necessarily converge nor produce a minimizer.

225 We begin by developing a weak formulation of the first order condition. Then, we describe multiple gradient flow schemes for finding (local) minimizers. The main purpose is to explain how different choices of the scheme (i.e. different implicit-explicit splittings) require different time step restrictions that are affected by the bulk and boundary parameters η and ω , and the twist parameter τ_0 . Many of the proofs are omitted, but can be found in [39].

3.1. First order condition

The minimization problem for the LdG energy functional (9), and associated first order condition, is

$$\bar{Q} = \arg \min_{Q \in \mathbf{V}} \mathcal{E}[Q], \quad \delta_Q \mathcal{E}[\bar{Q}; P] = 0, \quad \forall P \in \mathbf{V}, \quad (13)$$

235 where $\mathbf{V} := H^1(\Omega; \mathbf{S}_0)$ is the admissible space and $\delta_Q \mathcal{E}[\cdot; \cdot]$ is the variational derivative of $\mathcal{E}[\cdot]$. Next, we introduce various bilinear forms that will be convenient in our analysis and for numerical computation. Let $a_e(\cdot, \cdot) : \mathbf{V} \times \mathbf{V} \rightarrow \mathbb{R}$ be the bounded symmetric bilinear form defined by $a_e(Q, P) := \ell_1(Q_{ij,k}, P_{ij,k})_\Omega + \ell_2(Q_{ij,j}, P_{ik,k})_\Omega + \ell_3(Q_{ij,k}, P_{ik,j})_\Omega$. If ℓ_1, ℓ_2, ℓ_3 satisfy [23, Lem. 4.1]

$$0 < \ell_1, \quad -\ell_1 < \ell_3 < 2\ell_1, \quad -\frac{3}{5}\ell_1 - \frac{1}{10}\ell_3 < \ell_2, \quad (14)$$

240 then there is a constant $C > 0$ such that $a_e(P, P) \geq C\|\nabla P\|_{0,\Omega}^2$, for all $P \in \mathbf{V}$.

Next, let $a_s(\cdot, \cdot) : \mathbf{V} \times \mathbf{V} \rightarrow \mathbb{R}$ be the bounded symmetric bilinear form defined by $a_s(Q, P) := w_0(Q, P)_\Gamma + w_1(Q - Q^\perp, P)_\Gamma$, where $w_0, w_1 \geq 0$. If either w_0 or w_1 is positive, then there exists a constant $\alpha_1 > 0$ such that

$$a_e(P, P) + a_s(P, P) \geq \alpha_1 \|P\|_{1,\Omega}^2, \quad \forall P \in \mathbf{V}. \quad (15)$$

We also have the bilinear form $a_t(\cdot, \cdot) : \mathbf{V} \times \mathbf{V} \rightarrow \mathbb{R}$, which is *not* coercive, accounting for the twist term $a_t(Q, P) := 2\ell_1\tau_0 [\varepsilon_{ikl}(Q_{jk,l}, P_{ij})_\Omega + \varepsilon_{ikl}(P_{jk,l}, Q_{ij})_\Omega]$. For later use, we define one bilinear form to contain the previously defined forms:

$$a(Q, P) := a_e(Q, P) + a_t(Q, P) + a_s(Q, P),$$

and note that there is a constant $c_0 > 0$ such that $|a(Q, P)| \leq c_0 \|Q\|_{1,\Omega} \|P\|_{1,\Omega}$. We also introduce the linear form $l_{\text{rhs}}(\cdot) : \mathbf{V} \rightarrow \mathbb{R}$:

$$l_{\text{rhs}}(P) := (\chi(P), 1)_\Omega + w_0 (Q_\Gamma, P)_\Gamma + w_1 \left(-\frac{s_0}{3} \boldsymbol{\nu} \otimes \boldsymbol{\nu}, P \right)_\Gamma. \quad (16)$$

We can now write $\mathcal{E}[Q]$ in the form

$$\mathcal{E}[Q] = (1/2)a(Q, Q) + (1/\eta^2)(\psi(Q), 1)_\Omega + (1/\omega)(\phi(Q), 1)_\Gamma - l_{\text{rhs}}(Q),$$

²⁵⁰ which yields the following expression for the first variation of \mathcal{E} :

$$\delta_Q \mathcal{E}[Q; P] = a(Q, P) + (1/\eta^2)(D\psi(Q), P)_\Omega + (1/\omega)(D\phi(Q), P)_\Gamma - l_{\text{rhs}}(P).$$

Combining with (13), we find that \bar{Q} satisfies a tensor-valued, anisotropic, elliptic partial differential equation (PDE) *system* defined over Ω with a tensor-valued Robin boundary condition. For instance, in terms of indices $1 \leq i, j \leq 3$, the bulk PDE is

$$\begin{aligned} & -\ell_1 Q_{ij,kk} - \ell_2 Q_{ik,kj} - \ell_3 Q_{ik,jk} - 4\ell_1 \tau_0 \varepsilon_{i\ell k} Q_{\ell j,k} \\ & + \frac{1}{\eta^2} \left(-a_2 Q_{ij} - a_3 (Q^2)_{ij} + a_4 |Q|^2 Q_{ij} \right) = 0, \quad \text{in } \Omega, \end{aligned} \quad (17)$$

²⁵⁵ where only the traceless part of the tensor equation is considered. In (17), note that the term $4\ell_1 \tau_0 \varepsilon_{i\ell k} Q_{\ell j,k}$ is analogous to a convective term, e.g. $(V \cdot \nabla)Q$, where $V_{i\ell k} = 4\ell_1 \tau_0 \varepsilon_{i\ell k}$ is like a “velocity.” It is well known [40] that convection-diffusion problems present some difficulties in their numerical approximation, especially when the velocity is large. This is the case here when τ_0 is large, ²⁶⁰ which manifests as a mesh-size restriction in Thm. 5, as well as restricting the time-step when a popular convex-splitting scheme is used for finding an energy minimum (see Thm. 3).

3.2. Gradient Flow

²⁶⁵ We look for an energy minimizer using a gradient flow strategy [26, 29, 27, 22] applied to the energy (9). Let t represent “time” and suppose that $Q \equiv Q(x, t)$ evolves by an $L^2(\Omega)$ gradient flow:

$$(\partial_t Q(\cdot, t), P)_\Omega = -\delta_Q \mathcal{E}[Q; P], \quad \forall P \in \mathbf{V}, \quad (18)$$

where $Q(x, 0) = Q_0 \in \mathbf{V}$ is the initial guess for the flow. Formally, the solution of (18) will converge to a local minimizer. In this case, $Q(x, t)$ satisfies a parabolic PDE (in strong form), and by the standard theory of parabolic PDEs, it has ²⁷⁰ a unique solution. Gradient flows are related to the natural relaxation that many physical systems undergo, including LCs, which is why we use it in our

simulations. Directly minimizing \mathcal{E} by some other optimization technique is also possible and may yield other minimizers that are not commonly observed in experiment.

We discretize (18) in time by first letting $Q_k(x) \approx Q(x, k\delta t)$, where $\delta t > 0$ is a finite time-step and k is the time index. Next, we replace $\partial_t Q(\cdot, t)$ by a finite difference approximation, so then (18) becomes a sequence of elliptic problems. In other words, given Q_k , find $Q_{k+1} \in \mathbf{V}$ such that

$$\delta t^{-1} (Q_{k+1} - Q_k, P)_{\delta t} = -\delta_Q \mathcal{E}[Q_{k+1}; P], \quad \forall P \in \mathbf{V}, \quad (19)$$

where we have defined a time-stepping inner product $(\cdot, \cdot)_{\delta t}$ by

$$(P, T)_{\delta t} := \left(\frac{1}{\eta^2} \int_{\Omega} P : T + \frac{1}{\omega} \int_{\Gamma} P : T \right). \quad (20)$$

We also define a norm by $\|P\|_{\delta t}^2 := (P, P)_{\delta t}$. One can show that (19) is equivalent to a minimizing movements strategy [41]:

$$Q_{k+1} = \arg \min_{Q \in \mathbf{V}} \mathcal{F}^k(Q), \quad \mathcal{F}^k(Q) := \frac{1}{2\delta t} \|Q - Q_k\|_{\delta t}^2 + \mathcal{E}[Q], \quad (21)$$

which immediately yields the useful property $\mathcal{F}^k(Q_{k+1}) \leq \mathcal{F}^k(Q_k) \leq \mathcal{F}^{k-1}(Q_k)$ and implies that $\mathcal{E}[Q_{k+1}] \leq \mathcal{E}[Q_k]$ for all k . In practice, we iterate until we reach a final iteration index or some other stopping criteria (see Section 5.1). However, (19) is a *fully implicit* equation and requires an iterative solution because of the non-linearities in $\psi(Q)$ and $\phi(Q)$. The following theorem, whose proof can be found in [39], gives a time-step restriction to ensure energy decrease.

Theorem 2. *The sequence $\{Q_k\}_{k=0}^{\infty}$ defined by the method in (19) is monotonically energy decreasing, i.e. $\mathcal{E}[Q_{k+1}] \leq \mathcal{E}[Q_k]$, provided that $\delta t \leq 2/\max\{a_2 + a_3^2/a_4, 2s_0^2/3\}$.*

The time step restriction in Theorem 2 involves non-dimensional constants of $O(1)$. However, the time step inner product (20) used in (19) accounts for the strength of the non-convex terms through the positive constants η and ω . In other words, when either η and ω are small, the minimizing movements scheme in (21) penalizes $Q_{k+1} - Q_k$ to be small. Hence, the minimization sequence will take more iterations when either η and ω are small.

Other types of time-discretizations can be used, such as implicit-explicit methods. But they usually have more stringent time-step restrictions. Another related strategy is *convex-splitting* which is popular in gradient flow schemes [42, 27, 43]. For instance, let $\psi(Q) = \psi_c(Q) - \psi_e(Q)$, where ψ_c and ψ_e are convex functions of Q . We modify (19) by treating ψ_c implicitly and ψ_e explicitly. For simplicity, we drop the nonlinear ϕ term, and simplify the time stepping inner product to $(P, T)_{\delta t} = (P, T)_{\Omega}$. Then, (19) is replaced by the following. Given Q_k , find $Q_{k+1} \in \mathbf{V}$ such that

$$\begin{aligned} \delta t^{-1} (Q_{k+1} - Q_k, P)_\Omega + a(Q_{k+1}, P) + (1/\eta^2) (D\psi_c(Q_{k+1}), P)_\Omega \\ = l_{\text{rhs}}(P) + (1/\eta^2) (D\psi_e(Q_k), P)_\Omega, \quad \forall P \in \mathbf{V}. \end{aligned} \quad (22)$$

305 This scheme also has an energy decrease property with a time-step restriction.

Theorem 3. *The sequence $\{Q_k\}_{k=0}^\infty$ defined by the method in (22) is monotonically energy decreasing, i.e. $\mathcal{E}[Q_{k+1}] \leq \mathcal{E}[Q_k]$, provided that $\delta t \leq 2\alpha_1/(108\ell_1^2\tau_0^2 - \alpha_1^2)$, where α_1 is the coercivity constant in (15). If $|\tau_0| \leq \alpha_1/(2\sqrt{27}\ell_1)$, there is no restriction on δt .*

310 Usually, a convex splitting scheme is used to *avoid* a time-step restriction. However, the above discussion shows that a sufficiently large τ_0 will cause a restriction. Moreover, according to [43], a convex splitting scheme is nothing but a fully implicit scheme with time re-scaled (when $\tau_0 = 0$). Thus, we always use the fully implicit scheme as our gradient descent strategy to find a minimizer 315 of (13).

4. Finite Element Method

We approximate (19) by a finite element method [44]. In doing so, we assume that $\Omega \subset \mathbb{R}^3$ is discretized by a conforming shape regular triangulation $\mathcal{T}_h = \{T_i\}$ consisting of tetrahedra. Theorem 5 presents an error estimate for 320 our finite element discretization of the equilibrium problem (i.e. first order condition in (13)).

4.1. Spatial Discretization

325 Let $\mathbb{M}_h(\Omega_h)$ be the space of continuous, piecewise Lagrange polynomial functions on Ω_h , subordinate to the mesh \mathcal{T}_h of Ω_h , with polynomial degree ≥ 1 . We discretize (19) by approximating Q by a finite element function Q_h . Note that \mathbf{S}_0 can be uniquely identified with a five dimensional vector space [21], i.e. there exists 3×3 , symmetric traceless basis matrices $\{E^i\}_{i=1}^5$ such that any $Q \in \mathbf{S}_0$ can be uniquely expressed as $Q = q_i E^i$, for some coefficient functions q_1, \dots, q_5 . With this, we define the tensor finite element space

$$\mathbb{S}_h(\Omega_h) := \{P \in C^0(\Omega_h; \mathbf{S}_0) \mid P = q_{i,h} E^i, q_{i,h} \in \mathbb{M}_h(\Omega_h), 1 \leq i \leq 5\}, \quad (23)$$

330 and let $Q_h \in \mathbf{V}_h := \mathbb{S}_h(\Omega_h) \subset \mathbf{V}$. Thus, $Q_h = q_{i,h} E^i$, and $q_{i,h} \in H^1(\Omega)$ for $i = 1, \dots, 5$.

The fully discrete L^2 -gradient flow now follows from (19), i.e. given $Q_{h,k}$, find $Q_{h,k+1} \in \mathbf{V}_h$ such that

$$\delta t^{-1} (Q_{h,k+1} - Q_{h,k}, P_h)_{\delta t} = -\delta_Q \mathcal{E}[Q_{h,k+1}; P_h], \quad \forall P_h \in \mathbb{S}_h(\Omega_h), \quad (24)$$

We iterate this procedure until some stopping criteria is achieved (see Section 335 5.1). Since $\mathbf{V}_h \subset \mathbf{V}$, the same arguments in Section 3.2 still hold when replacing \mathbf{V} by \mathbf{V}_h . Therefore, the same time-stepping restrictions apply to the fully discrete formulation.

4.2. Error Estimate for the Equilibrium Problem

We present an error estimate for finite element approximations of a local minimizer of the LdG energy $\mathcal{E}[\cdot]$. If $Q \in \mathbf{V}$ is a local minimizer of $\mathcal{E}[\cdot]$, then it satisfies the first order condition in (13). Moreover, if $Q_h \in \mathbf{V}_h$ is a local minimizer of $\mathcal{E}[\cdot]$ (over the discrete space \mathbf{V}_h), then

$$\begin{aligned}\delta\mathcal{E}[Q_h](P_h) &= a(Q_h, P_h) + (1/\eta^2)(D\psi(Q_h), P_h)_\Omega \\ &\quad + (1/\omega)(D\phi(Q), P_h)_\Gamma - l_{\text{rhs}}(P_h) = 0, \quad \forall P_h \in \mathbf{V}_h.\end{aligned}\quad (25)$$

The error estimate in Theorem 5 is built on the following assumption, which says that the energy landscape around a minimizer is not too flat.

Assumption 4 (Isolated minimizer and coercivity). *For a given local minimizer Q of \mathcal{E} , we assume there exists $\zeta > 0$ such that for all \tilde{Q} with $\|Q - \tilde{Q}\|_{1,\Omega} < \zeta$, we have $\mathcal{E}[Q] \leq \mathcal{E}[\tilde{Q}]$, and for some $m_0 > 0$,*

$$\begin{aligned}\delta^2\mathcal{E}[\tilde{Q}](P, P) &= a(P, P) + (1/\eta^2)\left(P, D^2\psi(\tilde{Q})P\right)_\Omega \\ &\quad + (1/\omega)\left(P, D^2\phi(\tilde{Q})P\right)_\Gamma \geq m_0\|P\|_{1,\Omega}^2, \quad \forall P \in \mathbf{V}.\end{aligned}\quad (26)$$

In order to avoid additional technicalities, we assume that if Q is a solution of (13), then it has the additional regularity $Q \in H^2(\Omega)$. See [39] for further details.

Theorem 5. *Let $Q \in \mathbf{V}$ be a local minimizer of $\mathcal{E}[\cdot]$ that satisfies (13), and let $Q_h \in \mathbf{V}_h$ be a local minimizer of $\mathcal{E}[\cdot]$ that satisfies (25). Moreover, adopt Assumption 4 and assume that $\|Q - Q_h\|_{1,\Omega} < \zeta$. Then, there exists $c > 0$ such that for all $h \leq h_0$, we have $\|Q - Q_h\|_{1,\Omega} \leq ch\|Q\|_{2,\Omega}$, where*

$$h_0 = \frac{\sqrt{\alpha_1/(54\tau_0^2 + (\alpha_1/2) + a'(1/\eta^2) + (2/3)(1/\omega)s_0^2)}}{c_1(\ell_1 + 3\ell_2 + \ell_3 + 2\sqrt{27}\tau_0 + w_0 + 3w_1 + c_2(1/\eta^2) + c_3(1/\omega))}, \quad (27)$$

where c_1, c_2, c_3 and a' are $O(1)$ constants.

Note that (27) says that small values of η and ω , and large values of τ_0 , lead to small values of h_0 . Furthermore, this Theorem says there is *no* error estimate if the mesh size is too large. This means that the discrete problem may have *no* connection to the physical problem of interest.

5. Simulations

We present several simulations that illustrate the cholesteric Landau-de Gennes model on both a slab geometry and a spherical shell for a range of twist parameters. We illustrate both the richness of the model, as well as issues that can arise when the mesh size is not small enough. Our software is implemented in Firedrake [45], which heavily uses the PETSc library [46]. We used Paraview to visualize our simulations. We simulated on two of the machines owned by the LSU Department of Mathematics. Each machine was equipped with two Intel Xeon Gold 6242R processors running at 3.10/4.10 GHz, as well as a 768 GiB RAM. We ran our simulations on a single node using 25 processes.

³⁷⁰ 5.1. *Minimization technique*

As discussed in Section 3.2, the gradient descent method can be used to find a local minimizer of the LdG equilibrium problem. In our implementation, we apply this method to the finite element discretization of the problem. At each time step, we must solve a nonlinear system in (24), so Firedrake's builtin nonlinear solver (which utilizes Newton's method) is employed. We use the Geometric agglomerated Algebraic MultiGrid (GAMG) preconditioner, as well as the Minimal Residual Method (MINRES) for our Krylov subspace method.

However, the fully implicit gradient descent method we use comes with a time-step restriction (see Thm. 2) that is affected by η and ω through the minimizing movements inner product (21), as well as the twist τ_0 . This can lead to excessive computation times. Therefore, in practice, we start with a time-step that satisfies the various restrictions given earlier and compute several steps (e.g. we start with a time-step of $\delta t = 0.001$ and we compute 50 steps). Then, we increase the time-step by a factor of 10 and do several more steps (e.g. 50), checking that the energy continues to decrease with each step. If the energy does not decrease after increasing the time-step, or if the solver diverges, then we go back to the smaller time-step and perform more iterations before attempting to increase the time-step again. In practice, however, the energy always decreased in our simulations; the only situation in which we had to go back to the smaller time-step was when the solver diverged. This continues until δt reaches a maximum value of $\delta t = 100,000$, after which we continue iterating. During this procedure, for any value of δt , if the energy decrease between successive iterates is less than a tolerance (e.g. 10^{-6}), then we stop iterating and solve the equilibrium problem directly (i.e. no gradient descent). If the nonlinear solver for the equilibrium problem diverges, then we continue with several more gradient descent iterations. Despite the ad-hoc nature of this procedure, it was effective in obtaining (discrete) local minimizers of the discrete LdG energy in a reasonable amount of time.

³⁹⁵ 5.2. *Parameter choices and visualization*

The following parameter values were used for all simulations in Sections 5.3, 5.4, and 5.5. The coefficients of the double well in (5), were chosen as

$$a_0 = 1, \quad a_2 = 7.502104, \quad a_3 = 60.975813, \quad a_4 = 66.519069. \quad (28)$$

The function $\psi(Q)$ has a global minimum at $Q_* = s_0(\mathbf{1} \otimes \mathbf{1} - I/3)$, where $\mathbf{1} \in \mathbb{R}^3$ is any unit vector, and $s_0 = 0.7$. The other coefficients are given by $\ell_1 = 1.0$, $\ell_2 = \ell_3 = 0$, and $\eta = 0.1$. We conducted experiments with both homeotropic anchoring (i.e. $w_0 = 10.0$, $w_1 = w_2 = 0$) and planar degenerate anchoring (i.e. $w_0 = 0$, $w_1 = w_2 = 10.0$ and $\omega = 0.1$). The twist was varied, with values typically chosen as $\tau_0 = 0, 5, 10, 15, 20, 25$. In Section 5.6, a different set of parameters was used corresponding to the liquid crystal 5CB.

The numerical solution for Q is visualized by first performing an eigendecomposition of Q at each node of the mesh. We then set \mathbf{n} to be the eigenvector of Q corresponding to the largest eigenvalue of Q . If Q has a uniaxial form,

| τ_0 | Homeotropic anchoring | | Planar degenerate anchoring | |
|----------|-----------------------|---------------|-----------------------------|---------------|
| | Initial energy | Final energy | Initial energy | Final energy |
| 0 | 39.20061947 | 32.86058337 | 0.0 | 0.0 |
| 5 | 49.25887441 | -2.64966269 | 43.13556899 | -11.06811563 |
| 10 | 70.41495358 | -41.83731193 | 65.18722048 | -51.78216459 |
| 15 | 104.88188461 | -122.7420167 | 100.38078589 | -133.893747 |
| 20 | 151.32789951 | -254.83515683 | 147.15907691 | -265.87890179 |

Table 1: Energies for the slab ($2 \times 2 \times 0.2$) in Figure 3.

then this choice of \mathbf{n} is consistent with (2). Finally, we compute $|\mathbf{n} \cdot \mathbf{r}|$, where \mathbf{r} is a given vector that corresponds to the computational domain, and visualize $|\mathbf{n} \cdot \mathbf{r}|$ as a scalar field.

415 5.3. Slab Configuration

5.3.1. Experimental Setup

The domain Ω is a rectangular solid (slab geometry), where $\Omega = (0, 2) \times (0, 2) \times (0, 0.2)$. The boundary is partitioned as $\Gamma = \Gamma_1 \cup \Gamma_0$ where $\Gamma_1 = (0, 2) \times (0, 2) \times \{0, 0.2\}$ (top and bottom of the slab) and $\Gamma_0 = \Gamma \setminus \Gamma_1$ (sides of the slab). Then, in the formulation (19), we replace Γ with Γ_1 , i.e. we enforce the weak anchoring condition on Γ_1 and use a zero Neumann condition on Γ_0 . For the finite element discretized domain Ω_h , we chose a mesh size of $h = 0.02$.

The initial condition was chosen as follows. First, define

$$\mathbf{w}_1 = (0, \cos(\tau_0 x_1), \sin(\tau_0 x_1))^\dagger, \quad \mathbf{w}_2 = (\cos(\tau_0 x_2), \sin(\tau_0 x_2), 0)^\dagger. \quad (29)$$

Then for $i = 1, 2$ we define $\mathbf{n}_i = \mathbf{w}_i / |\mathbf{w}_i|$, and $Q_i := s_0(\mathbf{n}_i \otimes \mathbf{n}_i - I/3)$. Each Q_i corresponds to a helical configuration of the director field, with period given by $2\pi/\tau_0$. Then, choosing $\rho = (\cos(\tau_0 x_1) \cos(\tau_0 x_2) + 1)/2$, we set

$$Q_0 = (1 - \rho)Q_1 + \rho Q_2. \quad (30)$$

See Figure 3 for a visualization of the initial condition Q_0 and the computed local minimizers for both homeotropic and planar degenerate anchoring for a range of twist values τ_0 . Note that the color corresponds to $|\mathbf{n} \cdot \mathbf{r}|$ with $\mathbf{r} = \mathbf{e}_3$ (see Section 5.2).

5.3.2. Results

Table 1 lists the (non-dimensional) energies of the initial condition for each τ_0 compared to the energies of the equilibrium state (a local minimizer), for both homeotropic and planar degenerate anchoring. Figure 3 (middle column) depicts the final equilibrium solutions with homeotropic anchoring, all of which had very regular stripe patterns, except when $\tau_0 = 5$ where the solution for the homeotropic case consisted of the director pointing normal to the surface on the entire domain. In addition, as τ_0 increased, the final stripe patterns aligned more with the diagonal of the slab. This is most likely due to the zero Neumann condition imposed on the sides. If a periodic boundary condition were used, then the final configuration would be invariant to rotations of the $\mathbf{e}_1, \mathbf{e}_2$

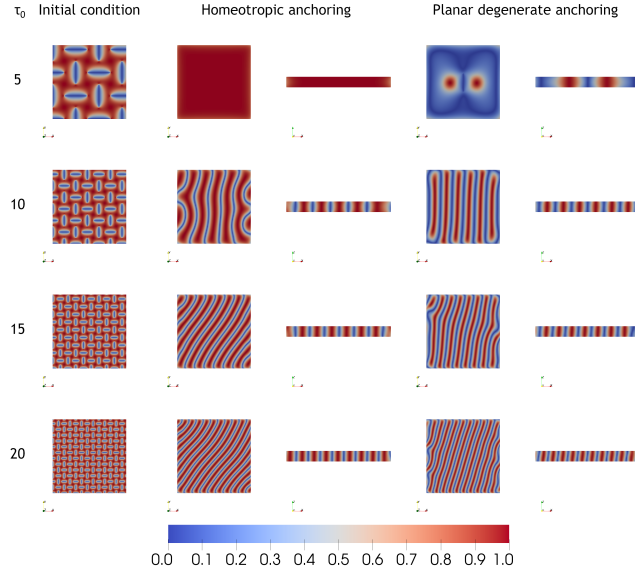


Figure 3: Slab geometry: $2 \times 2 \times 0.2$ (Sec. 5.3.2). Color is proportional to $|\mathbf{n} \cdot \mathbf{e}_3|$. Initial condition column shows top view of slab. Homeotropic anchoring columns show the top view and a vertical slice through the middle of the slab. Planar degenerate anchoring columns have the same format.

plane. We were not able to enforce this condition because of a limitation of Firedrake.

For the planar degenerate anchoring case (Figure 3, right column), similar striped patterns occurred in the equilibrium solutions for each twist value. However, the alignment with the diagonal was not quite as pronounced. Moreover, the transition between stripes was slightly different from the homeotropic case and the period was different. For instance, $\tau_0 = 20$ corresponds to an ideal period of $p = 2\pi/\tau_0 \approx 0.314$, but the measured period from the simulation was $p = 0.35$ ($p = 0.38$) for the homeotropic (planar degenerate) case. We also note that in the planar degenerate case, with $\tau_0 = 5$, the director is mainly tangential, except for two small, disconnected regions where the director becomes parallel to \mathbf{e}_3 . This is because the anchoring constants, which are set to $w_1 = w_2 = (1/\omega) = 10$, outweigh the twist. Simulation times varied, ranging from 0 to 41 hours for the homeotropic case, and 0 to 16 hours for the planar degenerate case. Times were generally shorter for the planar degenerate case.

5.4. Shell Configuration

5.4.1. Details

The domain Ω is a spherical annulus (shell), where two choices were used. For the first shell, we set $\Omega = \Omega_{\text{shell},0} := \mathcal{B}(\mathbf{0}, 1) \setminus \overline{\mathcal{B}}(\mathbf{0}, 0.9)$, where $\mathcal{B}(\mathbf{0}, r)$ is an open ball of radius r . For the finite element discretization Ω_h , we set the mesh size to be $h = 0.02$. For the initial condition, when $\tau_0 > 0$, we let

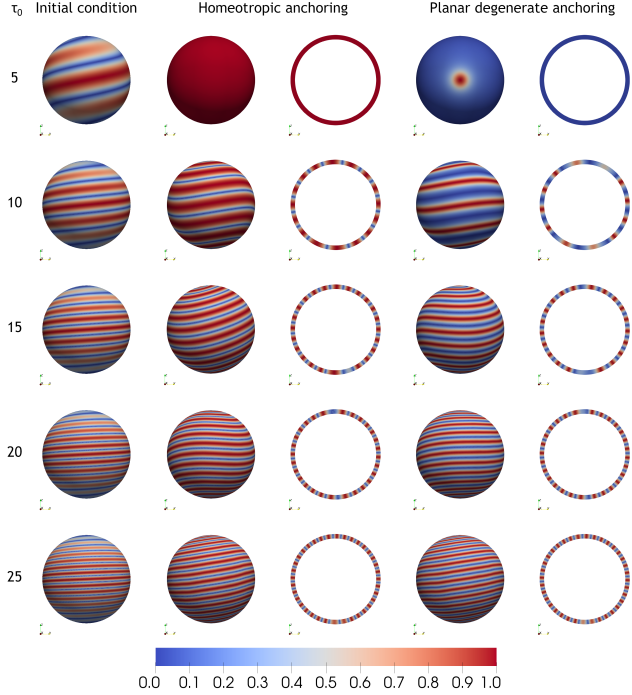


Figure 4: Centered shell ($\Omega_{\text{shell},0}$), front view (Sec. 5.4.2). Color is proportional to $|\mathbf{n} \cdot \mathbf{r}|$ with $\mathbf{r} = \mathbf{x}/|\mathbf{x}|$. Homeotropic anchoring columns show the outer boundary and a vertical slice through the shell. Planar degenerate anchoring columns have the same format.

$\mathbf{w} = \mathbf{w}(x_1, x_2, x_3) = (\cos(\tau_0 x_3), \sin(\tau_0 x_3), 0)^\dagger$. Then, similarly to the initial conditions for the slabs, we set $\mathbf{n} = \mathbf{w}/|\mathbf{w}|$ and

$$Q_0 = s_0 (\mathbf{n} \otimes \mathbf{n} - I/3). \quad (31)$$

For $\tau_0 = 0$, we let $\mathbf{n} = \mathbf{x}/|\mathbf{x}|$, and set Q_0 as in (31).

The far left column of Figures 4 and 5 depicts the initial condition, where the color corresponds to $|\mathbf{n} \cdot \mathbf{r}|$ with $\mathbf{r} = \mathbf{x}/|\mathbf{x}|$, i.e. the radial unit vector (see Section 5.2). The stripes in the initial condition form a spiral on the spherical boundary running top to bottom, with spacing inversely proportional to τ_0 . Moreover, Figures 4 and 5 show the final equilibrium state of Q , corresponding

| τ_0 | Homeotropic anchoring | | Planar degenerate anchoring | |
|----------|-----------------------|---------------|-----------------------------|---------------|
| | Initial energy | Final energy | Initial energy | Final energy |
| 0 | 1.23566209 | 1.23349847 | 56.94106826 | 51.13769725 |
| 5 | 60.49129983 | 1.23349741 | 12.23300007 | -13.13068291 |
| 10 | 21.34536007 | -33.76001607 | -26.81216759 | -62.48198396 |
| 15 | -36.59992963 | -151.97707415 | -84.58904161 | -185.01096392 |
| 20 | -103.25794942 | -348.22427414 | -151.0115368 | -384.49961726 |
| 25 | -166.11557298 | -639.23581796 | -213.57414074 | -677.04411588 |

Table 2: Energies for the centered shell ($\Omega_{\text{shell},0}$) in Figures 4 and 5.

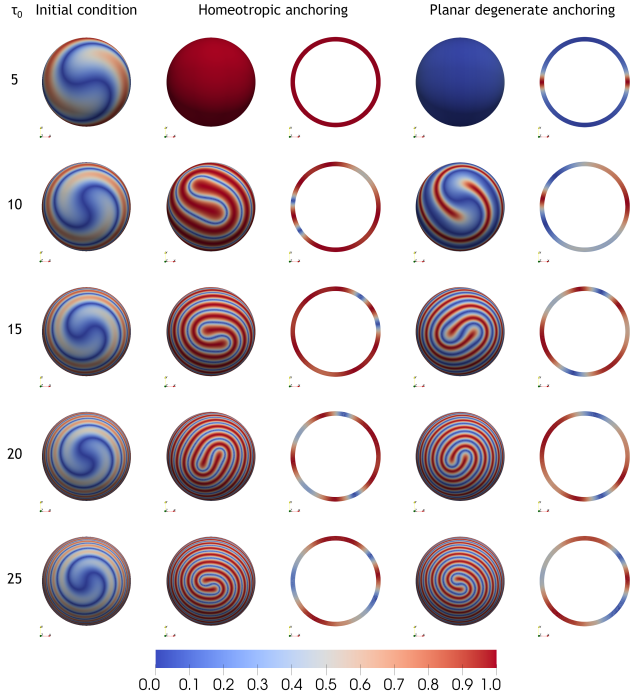


Figure 5: Centered shell ($\Omega_{\text{shell},0}$), top view (Sec. 5.4.2). Similar format to Figure 4; the slices are parallel to the view plane.

to a local minimizer, for both homeotropic and planar degenerate anchoring for a range of twist values τ_0 .

For the second shell, we set $\Omega = \Omega_{\text{shell},1} := \mathcal{B}(\mathbf{0}, 1) \setminus \bar{\mathcal{B}}(\mathbf{p}, 0.9)$, where $\mathbf{p} = (0, 0, 0.05)^\dagger$, i.e. an off-centered annulus. Our mesh size was again set to $h = 475$ 0.02. We used the same initial condition here as in (31). Figure 6 shows the initial condition, as well as the final equilibrium state, for a range of twist values.

We also performed another set of numerical experiments for the first shell, $\Omega = \Omega_{\text{shell},0}$, but with the initial condition set to Q_0 in (30). Figure 7 shows the initial condition, as well as the final equilibrium state, for a range of twist values. We omitted the case of $\tau_0 = 0$, since the results were not appreciably different from the previous experiments.

5.4.2. Results

We begin with the centered shell $\Omega_{\text{shell},0}$ and initial condition (31). Table 2 lists the (non-dimensional) energies of the initial condition for each τ_0 compared to the energies of the equilibrium state (a local minimizer), for both homeotropic and planar degenerate anchoring.

Figures 4 and 5 (middle column) depict the final equilibrium solutions with homeotropic anchoring, where the spiral stripe pattern has a slight undulation. Moreover, the spirals meet as two “fingers” at the poles of the shell. The slice

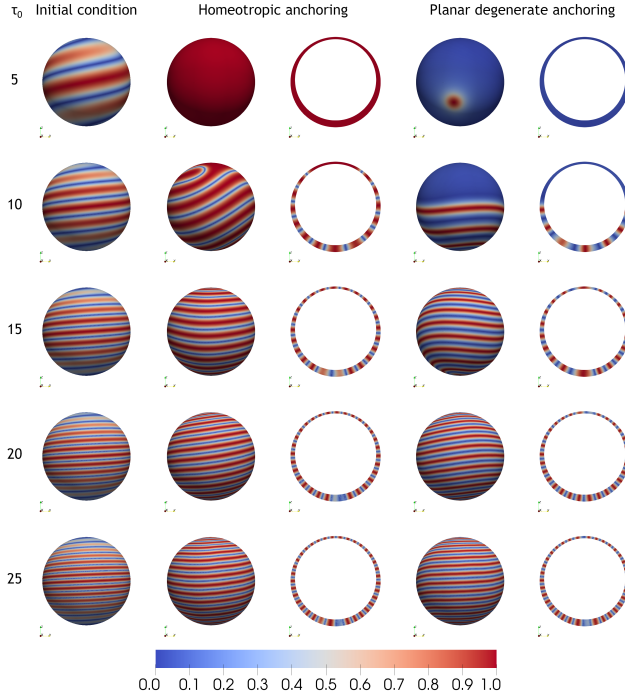


Figure 6: Off-centered shell ($\Omega_{\text{shell},1}$), front view (Sec. 5.4.2). Similar format to Figure 4.

| τ_0 | Homeotropic anchoring | | Planar degenerate anchoring | |
|----------|-----------------------|---------------|-----------------------------|---------------|
| | Initial energy | Final energy | Initial energy | Final energy |
| 0 | 1.34958562 | 1.26765658 | 56.95232872 | 1.56772626 |
| 05 | 60.4884546 | 1.24104888 | 12.23023189 | -13.2233694 |
| 10 | 21.30137144 | -34.07603296 | -26.85588133 | -64.03286781 |
| 15 | -36.81485612 | -149.89711829 | -84.80477055 | -182.77158029 |
| 20 | -103.91110362 | -342.9675383 | -151.66656546 | -379.13022842 |
| 25 | -167.63544101 | -630.70950725 | -215.09203743 | -668.63027357 |

Table 3: Energies for the off-centered shell ($\Omega_{\text{shell},1}$) in Figure 6.

views show that the spiral pattern persists through the shell’s thickness. For $\tau_0 = 5$, instead of a stripe pattern, the director \mathbf{n} is radial pointing outward from the origin, because the anchoring strength outweighs the twist effect.

For the planar degenerate anchoring case (Figures 4 and 5 (right column)), similar striped patterns are present in the equilibrium solutions for each twist value. We note that the transition between stripes is slightly different from the homeotropic case (as for the slab). For $\tau_0 = 5$, the director field is mainly tangential, except for two “poles” where the director becomes normal to the surface of the shell. Again, this is because the anchoring constants outweigh the twist.

Each simulation time ranged from 0 to 26 hours for the homeotropic case, and 0 to 11 hours for the planar degenerate case (with an exception for $\tau_0 = 10$ which

took nearly 20 hours). In general, higher twist correlates with longer simulation times, and the planar degenerate case took longer than the homeotropic case.

Next, we consider the off-centered shell $\Omega_{\text{shell},1}$ and initial condition (31).
505 Table 3 lists the (non-dimensional) energies of the initial condition for each τ_0 compared to the energies of the equilibrium state (a local minimizer), for both homeotropic and planar degenerate anchoring.

Figure 6 depicts the final equilibrium solutions for both homeotropic and planar degenerate anchoring, which show similar stripe patterns as for the previous centered shell. But there are some differences. For $\tau_0 = 5$ with planar degenerate anchoring, the two “poles” where the director becomes normal to the surface are shifted down toward the thicker part of the shell. For $\tau_0 = 10$ and homeotropic anchoring, the stripe pattern is absent at the top (thinnest) part of the shell; for planar degenerate, the spiral pattern is only present on the lower (thicker) half of the shell. For higher twists, the spiral patterns are similar to the previous (centered) shell. This is due to the interplay of the anchoring strength and the twist. Basically, there is not enough “room” in the thinnest part of the shell to develop a twist of the director field if τ_0 is not sufficiently large. Each simulation time ranged from 0 to 24 hours for the homeotropic case, and 2 to 80 hours for the planar degenerate case. In general, higher twist correlates with longer simulation times, and the planar degenerate case took longer than the homeotropic case. For example, with $\tau_0 = 0$, it took around 30 minutes for the homeotropic case, and 32 hours for the planar degenerate case.
510
515
520
525

| τ_0 | Homeotropic anchoring | | Planar degenerate anchoring | |
|----------|-----------------------|---------------|-----------------------------|---------------|
| | Initial energy | Final energy | Initial energy | Final energy |
| 5 | 107.21684588 | 1.23349885 | 65.88019321 | -12.85142139 |
| 10 | 143.69128926 | -33.21147874 | 103.37532314 | -66.79504813 |
| 15 | 198.33754579 | -151.71328798 | 158.2365114 | -185.18312273 |
| 20 | 269.46171783 | -348.4203652 | 229.41729719 | -384.3815465 |
| 25 | 352.2492802 | -639.0239269 | 312.42189391 | -676.81099557 |

Table 4: Energies for the centered shell ($\Omega_{\text{shell},0}$), with oscillatory initial condition, in Figures 7.

We now reconsider the centered shell $\Omega_{\text{shell},0}$ but with the initial condition (30).
525 Table 4 lists the (non-dimensional) energies of the initial condition for each τ_0 compared to the energies of the equilibrium state (a local minimizer), for both homeotropic and planar degenerate anchoring.

Figure 7 depicts the final equilibrium solutions for both homeotropic and planar degenerate anchoring, which show similar stripe patterns as before. However, the stripe patterns break away from being a spiral in some cases. For instance, with homeotropic anchoring and $\tau_0 = 15, 20$, we see multiple triple junctions of the blue region. In addition, we see similar triple junctions for the planar degenerate anchoring with $\tau_0 = 15$. The $\tau_0 = 10$ case (planar degenerate) exhibits a somewhat bizarre hexagonal/pentagonal pattern with a slightly lower energy than the minimizer in Figures 4 and 5 ($\mathcal{E} = -66.795$ vs. $\mathcal{E} = -62.482$).
530 Despite redoing this case with a finer mesh size of $h = 0.015$, the pattern persisted (with a final energy of $\mathcal{E} = -68.244$), suggesting that this may represent a true minimizer. The other cases exhibited a similar spiral pattern as before.
535

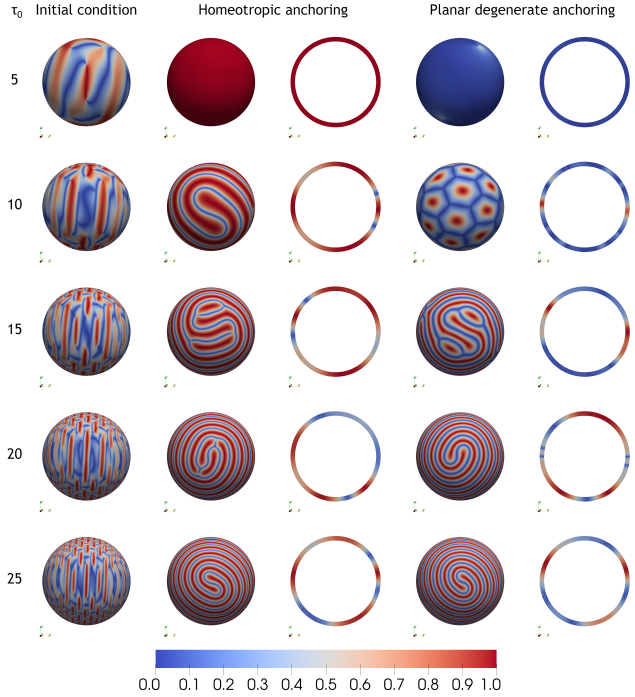


Figure 7: Centered shell ($\Omega_{\text{shell},0}$) with oscillatory initial condition, front view (Sec. 5.4.2). Similar format to Figure 4.

Each simulation took from 1 to 33 hours for the homeotropic case, and 4 to 14 hours for the planar degenerate case, with the latter case generally taking a shorter time than the former.

5.5. Comments on computing minimizers

We demonstrate the ramifications of Theorem 5, which has a mesh size restriction, on the form of discrete minimizers. Because of the non-convex terms in the energy, i.e. the double well and cholesteric term, the choice of mesh size affects more than just the resolution of the features of the minimizer Q . Indeed, too coarse a mesh can yield discrete minimizers that contain numerical artifacts, i.e. the ‘‘minimizer’’ may be very far from a true minimizer of the continuous problem. Figure 8(left) shows two simulations, one for the slab and one for shell, that illustrate how these numerical artifacts may manifest. In other words, when the mesh size is too large, the energy landscape of the discrete energy functional may contain artificial minima, so the gradient flow finds a different minimizer with a very different structure.

We also consider another type of perturbation of the initial condition in Figure 8(right). Here, a centered shell, with homeotropic anchoring, is considered with $\tau_0 = 15$, but the initial condition corresponds to $\tau_0 = 25$, i.e. more tightly packed stripes. Because of this mismatch of the initial condition, the simulation

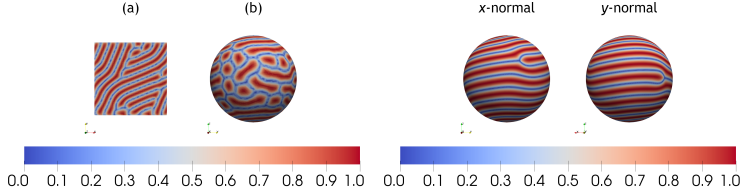


Figure 8: Left: Equilibrium states when the mesh size is not small enough (Sec. 5.5). Example (a) shows an energy minimizer, with $\mathcal{E} = -213.62$, for the large slab with the oscillatory initial condition and $\tau_0 = 20$, but with a mesh size of 0.05 (c.f. Figure 3 (homeotropic), with $\mathcal{E} = -254.84$, that used a mesh size of 0.02). Clearly, the period of the stripes in Figure 3 is much smaller than in (a) (to be exact, the period here is around 0.576). Example (b) shows a minimizer, with $\mathcal{E} = -757.69$, for the centered shell with the periodic initial condition and $\tau_0 = 25$, but with a mesh size of 0.05 and a shell thickness of 0.2 (c.f. Figure 4 (homeotropic), with $\mathcal{E} = -639.24$, that used a mesh size of 0.02 and a thickness of 0.1). Right: Different equilibrium states with mismatched initial condition (Sec. 5.5). We consider a centered shell with homeotropic anchoring and a twist of $\tau_0 = 15$ (recall Figure 4 (homeotropic)). However, we use a periodic initial condition consistent with $\tau_0 = 25$ (see far left col. in Figure 4), i.e. more stripes than the minimizer should have. The computed minimizer has energy $\mathcal{E} = -151.78$, compared to $\mathcal{E} = -151.98$ in Figure 4 (homeotropic), and contains two triple junctions not present in the previous simulation.

took approximately 1 week to “unwind” the extra twist in the initial condition to arrive at a minimizer with $\tau_0 = 15$. Moreover, the gradient flow obtained a different minimizer with a stripe pattern having two triple junctions, as opposed to Figure 4 which had no triple junctions.
560

5.6. Other Cholesteric Model

We attempted to reproduce a result of Lavrentovich and Tran in [12, Fig. 6], which models a cholesteric shell with outer radius $0.42 \mu\text{m}$ and inner radius $0.24 \mu\text{m}$. From this, we choose the characteristic length $\xi = 0.42 \mu\text{m}$.
565

The dimensional parameters used are for the 5CB liquid crystal, which can be found in [29]. The double well constants are $a_2 = 0.172 \times 10^6 \text{ J/m}^3$, $a_3 = 2.12 \times 10^6 \text{ J/m}^3$, and $a_4 = 1.73 \times 10^6 \text{ J/m}^3$. Following Section 2.3, we then calculate $c_0 = 0.038362224 \times 10^6 \text{ J/m}^3$, and divide the double well coefficients by c_0 to obtain the non-dimensional double well:
570

$$a_0 = 1.0, \quad a_2 = 4.4835774, \quad a_3 = 55.262698, \quad a_4 = 45.096447,$$

which gives $s_0 = 0.7992969$.

For the elastic coefficients (for 5CB in [29]), we have $\check{\ell}_1 = \check{\ell}_2 = 4 \times 10^{-11} \text{ J/m}$, $\check{\ell}_{24} = 0$. Since $\check{\ell}_{24} = 0$, this corresponds, via the mapping of the constants in Section 2.4, to $\ell_1 = \ell_2 = 4 \times 10^{-11} \text{ J/m}$, $\ell_3 = -4 \times 10^{-11} \text{ J/m}$. From here, we choose $\ell_m = 4 \times 10^{-11} \text{ J/m}$ and divide by ℓ_m to obtain $\ell_1 = \ell_2 = 1$, $\ell_3 = -1$. Note that the inequalities in (14) are not strictly satisfied in this case. We also have a cholesteric pitch of $p = 0.18 \mu\text{m}$, and so the non-dimensional twist is $\tau_0 = 14.660766$. The anchoring condition is planar degenerate with $w_0 = 0$, $w_1 = 4 \times 10^{-4} \text{ J/m}^2$, $w_2 = 8 \times 10^{-4} \text{ J/m}^2$. Multiplying the first two by ξ/ℓ_m ,
575

580 we obtain $w_0 = 0$, $w_1 = 4.2$. Finally, using the formulas $\eta = \sqrt{\ell_m/(c_0\xi^2)}$ and $\omega = \ell_m/(w_2\xi)$, we have that $\eta = 0.07688273$ and $\omega = 0.11904762$.

585 We ran simulations for the above parameters using the following three models: A, B-1, B-2. Model A is given in (3) (see [9, 10, 29]), and model B-1 is the cholesteric model in [11] and discussed in Section 2.4. Since s_0 is inconsistent with their *effective* double well $\tilde{\psi}$ (see Section 2.4.2, and the discussion about the extra $\text{tr}(Q^2)$ term), we ran the simulation for a model B-2, which is identical to B-1, except that we replace s_0 with the correct global minimum \tilde{s}_0 for $\tilde{\psi}$.

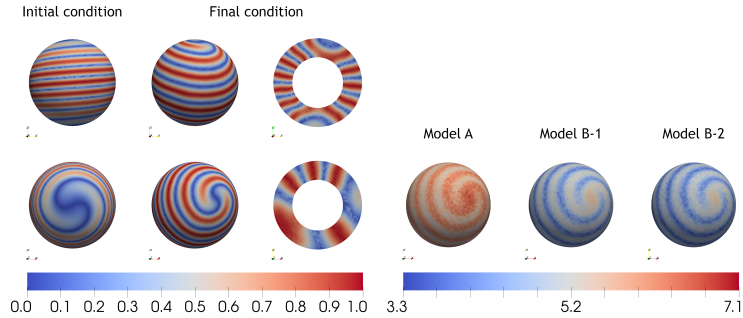


Figure 9: Left: Results from the simulation of Model A (Sec. 5.6). Both a front view and a top view are shown, with a view of the initial condition and final state (both outside view and slice are shown). Models B-1 and B-2 had visually indistinguishable patterns. Right: Results from the simulation of Models A, B-1, B-2 (Sec. 5.6), except viewing the largest eigenvalue $\bar{\lambda} = \max\{\lambda_i\}_{i=1}^3$ of the energy minimizing Q . We have Model A (our formulation), Model B-1, (their formulation with their inconsistent s_0), and Model B-2 (their formulation with a consistent s_0).

| Model | Initial energy | Final energy |
|-------|----------------|---------------|
| A | -196.83349123 | -479.36144656 |
| B-1 | 310.00570697 | 185.52404418 |
| B-2 | 365.134880212 | 183.86282819 |

Table 5: Energies for the model comparisons in Figure 9 (Sec. 5.6).

590 The energy results of these simulations are found in Table 5, and the results of the simulation using model A are found in Figure 9(left), which does not exactly match the result in [12, Fig. 6]. Their method uses a conjugate gradient method which is different from our minimization scheme, i.e. their method travels along a different path in the energy landscape so finds a different local minimizer.

595 We do not give the visualization of the other two models (B-1, B-2), because they look *nearly identical* to Model A. We suspect this is due to the cholesteric twist having a dominant effect. It should be noted, however, that models A and B-1, B-2 differ greatly in their final energies, as well as in the values of the maximum eigenvalue $\bar{\lambda}$ of Q , the latter of which is shown in Figure 9(right). We emphasize that, due to the energetic differences, if other physics were to be 600 coupled to the liquid crystal (e.g. electro-static effects), then the models would

most likely give vastly different equilibrium states.

It took approximately 2 hours to simulate model A, while it took about 40 minutes to simulate models B-1 and B-2. The mesh size used was 0.04285714.

6. Conclusions

The first part of this paper gives an overview of the Landau-de Gennes (LdG) model [9, 10, 29] for nematic LCs, with cholesteric effects, and connects it to a slightly different cholesteric model in [11]. We then presented a gradient flow and numerical scheme for the cholesteric LdG model, while noting important time-step restrictions to have an energy decreasing algorithm. Moreover, we gave a mesh size restriction that ensures that discrete minimizers are approximate versions of isolated, true minimizers.

Using our gradient flow, we compute (local) minimizers with an adaptive time-stepping strategy to reduce the computation time. This produced several numerical simulations that illustrate the rich behavior of the cholesteric LdG model. For both slab and shell geometries, the minimizer has regular stripe patterns that are affected by the domain shape. Specifically, the off-centered shell has a very different minimizer than the centered shell for intermediate values of the twist τ_0 . We also demonstrate that our gradient flow scheme can compute different (local) minimizers for the same set of parameters but depending on the initial condition. Some of the simulations show perturbed stripe patterns that exhibit “triple junctions” of the stripe and are due to using initial conditions with a high spatial frequency. All of these (equilibrium) stripe patterns are inline with known experiments for cholesteric LCs [11, 12, 16, 17].

We also gave examples of how artificial solutions may arise if the mesh size is not small enough, i.e. the computed minimizer may exhibit discrete artifacts. Furthermore, we showed that the two cholesteric models exhibit very different energies, though the computed solution may still have a very similar configuration of the director \mathbf{n} .

The results of this paper should help inform LC computational scientists about potential pitfalls in the simulation of the cholesteric LdG model and lead to more robust numerical predictions of cholesteric LC physics.

References

- [1] I. W. Hamley, Nanotechnology with soft materials, *Angewandte Chemie International Edition* 42 (15) (2003) 1692–1712. doi:10.1002/anie.200200546.
- [2] G. Ozin, I. Manners, S. Fournier-Bidoz, A. Arsenault, Dream nanomachines, *Advanced Materials* 17 (24) (2005) 3011–3018.
- [3] P. G. de Gennes, J. Prost, *The Physics of Liquid Crystals*, 2nd Edition, Vol. 83 of *International Series of Monographs on Physics*, Oxford Science Publication, Oxford, UK, 1995.
- [4] L. Blinov, *Electro-optical and magneto-optical properties of liquid crystals*, Wiley, 1983.
- [5] J. W. Goodby, *Handbook of Visual Display Technology* (Editors: Chen, Janglin, Cranton, Wayne, Fihn, Mark), Springer, 2012, Ch. Introduction to Defect Textures in Liquid Crystals, pp. 1290–1314.
- [6] J. Sun, H. Wang, L. Wang, H. Cao, H. Xie, X. Luo, J. Xiao, H. Ding, Z. Yang, H. Yang, Preparation and thermo-optical characteristics of a smart polymer-stabilized liquid crystal thin film based on smectic A-chiral nematic phase transition, *Smart Materials and Structures* 23 (12) (2014) 125038.
URL <http://stacks.iop.org/0964-1726/23/i=12/a=125038>
- [7] J. Hoogboom, J. A. Elemans, A. E. Rowan, T. H. Rasing, R. J. Nolte, The development of self-assembled liquid crystal display alignment layers, *Philosophical Transactions of the Royal Society of London A: Mathematical, Physical and Engineering Sciences* 365 (1855) (2007) 1553–1576. doi:10.1098/rsta.2007.2031.
- [8] P. Dasgupta, M. K. Das, B. Das, Fast switching negative dielectric anisotropic multicomponent mixtures for vertically aligned liquid crystal displays, *Materials Research Express* 2 (4) (2015) 045015.
URL <http://stacks.iop.org/2053-1591/2/i=4/a=045015>
- [9] H. Mori, J. Eugene C. Gartland, J. R. Kelly, P. J. Bos, Multidimensional director modeling using the Q-tensor representation in a liquid crystal cell and its application to the π -cell with patterned electrodes, *Japanese Journal of Applied Physics* 38 (1R) (1999) 135–146.
URL <http://stacks.iop.org/1347-4065/38/i=1R/a=135>
- [10] N. J. Mottram, C. J. P. Newton, Introduction to Q-tensor theory, ArXiv e-prints (Sep. 2014). arXiv:1409.3542.
- [11] L. Tran, M. O. Lavrentovich, G. Durey, A. Darmon, M. F. Haase, N. Li, D. Lee, K. J. Stebe, R. D. Kamien, T. Lopez-Leon, Change in stripes

- 670 for cholesteric shells via anchoring in moderation, *Phys. Rev. X* 7 (2017) 041029. doi:[10.1103/PhysRevX.7.041029](https://doi.org/10.1103/PhysRevX.7.041029).
URL <https://link.aps.org/doi/10.1103/PhysRevX.7.041029>
- 675 [12] M. O. Lavrentovich, L. Tran, Undulation instabilities in cholesteric liquid crystals induced by anchoring transitions, *Phys. Rev. Research* 2 (2020) 023128. doi:[10.1103/PhysRevResearch.2.023128](https://doi.org/10.1103/PhysRevResearch.2.023128).
URL <https://link.aps.org/doi/10.1103/PhysRevResearch.2.023128>
- 680 [13] Z. Dogic, S. Fraden, Ordered phases of filamentous viruses, *Current Opinion in Colloid & Interface Science* 11 (1) (2006) 47–55. doi:<https://doi.org/10.1016/j.cocis.2005.10.004>.
URL <https://www.sciencedirect.com/science/article/pii/S1359029405000981>
- 685 [14] D. X. Oh, Y. J. Cha, H.-L. Nguyen, H. H. Je, Y. S. Jho, D. S. Hwang, D. K. Yoon, Chiral nematic self-assembly of minimally surface damaged chitin nanofibrils and its load bearing functions, *Scientific Reports* 6 (1) (2016) 23245. doi:[10.1038/srep23245](https://doi.org/10.1038/srep23245).
URL <https://doi.org/10.1038/srep23245>
- 690 [15] G. Agez, C. Bayon, M. Mitov, Multiwavelength micromirrors in the cuticle of scarab beetle *chrysina gloriosa*, *Acta Biomaterialia* 48 (2017) 357–367. doi:<https://doi.org/10.1016/j.actbio.2016.11.033>.
URL <https://www.sciencedirect.com/science/article/pii/S1742706116306298>
- 695 [16] J. P. Lagerwall, G. Scalia, A new era for liquid crystal research: Applications of liquid crystals in soft matter nano-, bio- and microtechnology, *Current Applied Physics* 12 (6) (2012) 1387 – 1412. doi:<https://doi.org/10.1016/j.cap.2012.03.019>.
URL <http://www.sciencedirect.com/science/article/pii/S1567173912001113>
- 700 [17] M. Schwartz, G. Lenzini, Y. Geng, P. B. Rønne, P. Y. A. Ryan, J. P. F. Lagerwall, Cholesteric liquid crystal shells as enabling material for information-rich design and architecture, *Advanced Materials* 30 (30) (2018) 1707382. arXiv:<https://onlinelibrary.wiley.com/doi/pdf/10.1002/adma.201707382>, doi:[10.1002/adma.201707382](https://doi.org/10.1002/adma.201707382).
URL <https://onlinelibrary.wiley.com/doi/abs/10.1002/adma.201707382>
- 705 [18] A. M. Martinez, M. K. McBride, T. J. White, C. N. Bowman, Reconfigurable and spatially programmable chameleon skin-like material utilizing light responsive covalent adaptable cholesteric liquid crystal elastomers, *Advanced Functional Materials* 30 (35) (2020) 2003150. arXiv:<https://onlinelibrary.wiley.com/doi/pdf/10.1002/adfm.202003150>, doi:<https://doi.org/10.1002/adfm.202003150>.

- URL <https://onlinelibrary.wiley.com/doi/abs/10.1002/adfm.202003150>
- [19] Y. Geng, R. Kizhakidathazhath, J. P. F. Lagerwall, Robust cholesteric liquid crystal elastomer fibres for mechanochromic textiles, *Nature Materials* 21 (12) (2022) 1441–1447. doi:[10.1038/s41563-022-01355-6](https://doi.org/10.1038/s41563-022-01355-6).
 URL <https://doi.org/10.1038/s41563-022-01355-6>
- [20] J. Lagerwall, Liquid crystal elastomer actuators and sensors: Glimpses of the past, the present and perhaps the future, *Programmable Materials* 1 (2023) e9. doi:[10.1017/pma.2023.8](https://doi.org/10.1017/pma.2023.8).
- [21] E. C. Gartland Jr, P. Palffy-Muhoray, R. S. Varga, Numerical minimization of the Landau-de Gennes free energy: Defects in cylindrical capillaries, *Molecular Crystals and Liquid Crystals* 199 (1) (1991) 429–452.
- [22] I. Bajc, F. Hecht, S. Žumer, A mesh adaptivity scheme on the Landau-de Gennes functional minimization case in 3D, and its driving efficiency, *Journal of Computational Physics* 321 (2016) 981 – 996. doi:<https://doi.org/10.1016/j.jcp.2016.02.072>.
 URL <http://www.sciencedirect.com/science/article/pii/S0021999116001443>
- [23] T. Davis, E. Gartland, Finite element analysis of the Landau-de Gennes minimization problem for liquid crystals, *SIAM Journal on Numerical Analysis* 35 (1) (1998) 336–362. arXiv:<https://doi.org/10.1137/S0036142996297448>, doi:[10.1137/S0036142996297448](https://doi.org/10.1137/S0036142996297448).
 URL <https://doi.org/10.1137/S0036142996297448>
- [24] S. Bartels, A. Raisch, Simulation of Q-tensor fields with constant orientational order parameter in the theory of uniaxial nematic liquid crystals, in: M. Griebel (Ed.), *Singular Phenomena and Scaling in Mathematical Models*, Springer International Publishing, 2014, pp. 383–412. doi:[10.1007/978-3-319-00786-1_17](https://doi.org/10.1007/978-3-319-00786-1_17).
- [25] J.-P. Borthagaray, R. H. Nochetto, S. W. Walker, A structure-preserving FEM for the uniaxially constrained **Q**-tensor model of nematic liquid crystals, *Numerische Mathematik* 145 (2020) 837 – 881. doi:[10.1007/s00211-020-01133-z](https://doi.org/10.1007/s00211-020-01133-z).
 URL <https://doi.org/10.1007/s00211-020-01133-z>
- [26] G.-D. Lee, J. Anderson, P. J. Bos, Fast Q-tensor method for modeling liquid crystal director configurations with defects, *Applied Physics Letters* 81 (21) (2002) 3951–3953. arXiv:<https://doi.org/10.1063/1.1523157>, doi:[10.1063/1.1523157](https://doi.org/10.1063/1.1523157).
 URL <https://doi.org/10.1063/1.1523157>
- [27] J. Zhao, Q. Wang, Semi-discrete energy-stable schemes for a tensor-based hydrodynamic model of nematic liquid crystal flows, *Journal of Scientific*

- Computing 68 (3) (2016) 1241–1266. doi:[10.1007/s10915-016-0177-x](https://doi.org/10.1007/s10915-016-0177-x).
URL <https://doi.org/10.1007/s10915-016-0177-x>
- [28] J. Zhao, X. Yang, J. Shen, Q. Wang, A decoupled energy stable scheme for a hydrodynamic phase-field model of mixtures of nematic liquid crystals and viscous fluids, Journal of Computational Physics 305 (2016) 539 – 556. doi:<https://doi.org/10.1016/j.jcp.2015.09.044>.
URL <http://www.sciencedirect.com/science/article/pii/S0021999115006439>
- [29] M. Ravnik, S. Žumer, Landau-degennes modelling of nematic liquid crystal colloids, Liquid Crystals 36 (10-11) (2009) 1201–1214.
arXiv:<https://doi.org/10.1080/02678290903056095>, doi:[10.1080/02678290903056095](https://doi.org/10.1080/02678290903056095).
URL <https://doi.org/10.1080/02678290903056095>
- [30] S. Čopar, M. Ravnik, S. Žumer, Janus nematic colloids with designable valence, Materials 7 (6) (2014) 4272. doi:[10.3390/ma7064272](https://doi.org/10.3390/ma7064272).
URL <http://www.mdpi.com/1996-1944/7/6/4272>
- [31] E. G. Virga, Variational Theories for Liquid Crystals, 1st Edition, Vol. 8, Chapman and Hall, London, 1994.
- [32] A. Majumdar, Equilibrium order parameters of nematic liquid crystals in the landau-de gennes theory, European Journal of Applied Mathematics 21 (2) (2010) 181–203. doi:[10.1017/S0956792509990210](https://doi.org/10.1017/S0956792509990210).
- [33] A. M. Sonnet, E. Virga, Dissipative Ordered Fluids: Theories for Liquid Crystals, Springer, 2012.
- [34] G. Barbero, G. Durand, On the validity of the rapini-papoulier surface anchoring energy form in nematic liquid crystals, J. Phys. France 47 (12) (1986) 2129–2134. doi:[10.1051/jphys:0198600470120212900](https://doi.org/10.1051/jphys:0198600470120212900).
URL <https://doi.org/10.1051/jphys:0198600470120212900>
- [35] S. W. Walker, On The Correct Thermo-dynamic Potential for Electro-static Dielectric Energy, arXiv 1803.08136 (mar 2018). arXiv:[1803.08136](https://arxiv.org/abs/1803.08136).
- [36] R. P. Feynman, R. B. Leighton, M. Sands, The Feynman Lectures on Physics, Addison-Wesley Publishing Company, 1964.
- [37] P. Biscari, P. Cesana, Ordering effects in electric splay freedericksz transitions, Continuum Mechanics and Thermodynamics 19 (5) (2007) 285–298. doi:[10.1007/s00161-007-0055-8](https://doi.org/10.1007/s00161-007-0055-8).
- [38] J. Eugene C. Gartland, Scalings and limits of landau-de gennes models for liquid crystals: a comment on some recent analytical papers, Mathematical Modelling and Analysis 23 (3) (2018) 414 – 432. doi:<https://doi.org/10.3846/mma.2018.025>.

- [39] A. Hicks, Modeling and numerical analysis of the cholesteric landau-de
790 gennes model, Ph.D. thesis.
- [40] M. Stynes, D. Stynes, Convection Diffusion Problems: An Introduction to
Their Analysis and Numerical Solution, Graduate Studies in Mathematics,
AMS.
- [41] G. D. Maso, M. Forti, M. Miranda, S. A. Spagnolo, L. Ambrosio (Eds.), Se-
795 lected Papers, Springer Collected Works in Mathematics, Ennio De Giorgi,
2006.
- [42] S. M. Wise, C. Wang, J. S. Lowengrub, An energy-stable and convergent
finite-difference scheme for the phase field crystal equation, SIAM J. Nu-
mer. Anal. 47 (3) (2009) 2269–2288. doi:10.1137/080738143.
- [43] J. Xu, Y. Li, S. Wu, A. Bousquet, On the stability and accuracy of
800 partially and fully implicit schemes for phase field modeling, Computer
Methods in Applied Mechanics and Engineering 345 (2019) 826 – 853.
doi:<https://doi.org/10.1016/j.cma.2018.09.017>.
URL [http://www.sciencedirect.com/science/article/pii/
805 S0045782518304687](http://www.sciencedirect.com/science/article/pii/S0045782518304687)
- [44] S. C. Brenner, L. R. Scott, The Mathematical Theory of Finite Element
Methods, 3rd Edition, Vol. 15 of Texts in Applied Mathematics, Springer,
New York, NY, 2008.
- [45] F. Rathgeber, D. A. Ham, L. Mitchell, M. Lange, F. Luporini, A. T. T.
810 Mcrae, G.-T. Bercea, G. R. Markall, P. H. J. Kelly, Firedrake: Automating
the finite element method by composing abstractions, ACM Trans. Math.
Softw. 43 (3) (dec 2016). doi:10.1145/2998441.
URL <https://doi.org/10.1145/2998441>
- [46] S. Balay, S. Abhyankar, M. F. Adams, J. Brown, P. Brune, K. Buschelman,
815 L. Dalcin, V. Eijkhout, W. D. Gropp, D. Kaushik, M. G. Knepley, L. C.
McInnes, K. Rupp, B. F. Smith, S. Zampini, H. Zhang, H. Zhang, PETSc
Web page, <http://www.mcs.anl.gov/petsc> (2016).
URL <http://www.mcs.anl.gov/petsc>